

## Effect of short-range order on lattice distortion, stacking fault energy, and mechanical performance of Co-Fe-Ni-Ti high-entropy alloy at finite temperature

Xianteng Zhou <sup>1</sup>, Hongquan Song <sup>2</sup>, Chaokun Guo,<sup>1</sup> Zhen Yang <sup>1</sup>, and Fuyang Tian <sup>1,\*</sup>

<sup>1</sup>*Institute of Applied Physics and Department of Physics, University of Science and Technology Beijing, Beijing, 100083, China*

<sup>2</sup>*College of Physics and Telecommunication Engineering, Zhoukou Normal University, Zhoukou 466001, China*



(Received 5 December 2023; accepted 29 April 2024; published 15 May 2024)

The characterization of short-range order (SRO) and its influence on performance are a widely debated topics in high-entropy alloys (HEAs). In this work, taking the Co-Fe-Ni-Ti alloy without complicated magnetism as a benchmark of 3d HEAs, we investigate the effect of SRO on local lattice distortion (LLD), general stacking fault energy (GSFE), tensile and shear strength of FCC  $\text{Co}_{30}\text{Fe}_{16.66}\text{Ni}_{36.67}\text{Ti}_{16.67}$  via the combination of Monte Carlo (MC) and molecular dynamics (MD). This alloy shows the typical SRO of Ti-X ( $X = \text{Fe}, \text{Co}$ ) atomic pairs, while the segregation of Ti-Ti atomic pairs. The SRO has a minor inhibition on LLD. Considering the thermal vibration induced atomic displacement, the degree of LLD increases nonlinearly with increasing temperature. Both the severe LLD and SRO are helpful to tune the GSFE at finite temperature. The SRO enhances the degree of deformation twinning and delays the appearance of the HCP phase but increases the number of HCP-type atoms as the energy buffers. For the polycrystalline systems, SRO promotes the precipitation of BCC phase at grain boundaries and the number of HCP-type atoms in the grain and activates the deformation of slip surfaces. Therefore SRO could play a key role for the outstanding strength and plasticity of Co-Fe-Ni-Ti HEAs.

DOI: [10.1103/PhysRevMaterials.8.053602](https://doi.org/10.1103/PhysRevMaterials.8.053602)

### I. INTRODUCTION

In 2004, Yeh and Cantor *et al.* proposed an innovative alloying concept, delineating the emergence of a distinct alloy class characterized by the inclusion of five or more nearly equiatomic concentrations of metallic elements [1,2]. This concept laid the foundation for what is now recognized as high-entropy alloys (HEAs), also known as multiprincipal or multicomponent alloys [3–5]. Both the challenging scientific questions and extraordinary properties in HEAs highly attract the increasing prominence in the scientific and industrial communities. It is still difficult to characterize accurately the temperature dependent short-range order (SRO), local lattice distortion (LLD), and stacking fault energy (SFE) for face center cubic (FCC) HEAs. It could be due to the thermodynamic and kinetic properties on the FCC HEAs composed of 3d or 4d magnetic elements strongly influenced by magnetic ordering, excitation, and transition as well as spin coupling with other degrees of freedom.

Initially, researchers held the belief that the atomic distribution in HEAs was random. The ideal chemical disorder induced high configuration entropy keeps HEAs in the formation of a single-phase solid solution. The recent experimental and theoretical findings have provided the evidence of the SRO presence in FCC HEAs [6–9], whereas, Yin *et al.*'s results suggest that SRO in CoCrNi is either negligible or has no systematic measurable effect on strength [10]. The distribution of five constituent elements in CoCrFeMnNi HEA is relatively random and uniform, while CoCrFeNiPd shows the

great aggregation, with a wavelength of incipient concentration waves, as small as 1–3 nanometer [11]. One argues if the intrinsic stacking fault energy (ISFE) is positive or negative [12,13], and how SRO and temperature influence the ISFE [14,15] for FCC HEAs. In addition, the LLD degree in FCC HEAs is considered to be less severe, whereas LLD depends on the neighboring atomic environment [16–19], further could be changed by SRO [20]. How to describe quantitatively the SRO induced LLD and general stacking fault energy (GSFE) at finite temperature is still lacking [15].

The atomic size difference and electronegativity between metallic elements could lead to the elemental segregation and atomic clustering. Considering that FCC HEAs composed of early and last 3d transition elements exist relatively strong affinity, we take the FCC Co-Fe-Ni-Ti HEA as a benchmark model to study the influences of SRO. The Co-Fe-Ni-Ti alloy, different from FCC HEAs containing Cr and Mn [21,22], has no the complicated magnetic properties and magneto-acoustic coupling, and further could not result in the less accuracy of computations at atomistic simulations. Furthermore, the validation of model interatomic potentials (Zhou's potentials [23]) on the quaternary CoFeNiTi HEA has been verified [24,24–27]. Based on Zhou's potentials, the molecular dynamics (MD) simulation of shear deformation for FCC  $\text{Co}_{30}\text{Fe}_{16.66}\text{Ni}_{36.67}\text{Ti}_{16.67}$  is in good agreement with the experimental yield strength for an analogous FCC concentrated solid solution alloy [24]. The predicted SRO was used to quantify and validate the extension of high-concentration solid solution analytic models for FCC and body center cubic (BCC) Co-Fe-Ni-Ti HEAs [25,28].

The extensive research has been conducted on equimolar HEAs composed of early and last 3d metallic elements,

\*fuyang@ustb.edu.cn

such as CoCrFeMnNi [2], CoCrFeNi [29,30], CoCrNi [8,31], CoFeNiV [32], and CoNiV [33,34], for instance, Li *et al.* proposed that the different phases containing FCC and BCC play distinct roles in enhancing both the strength and plasticity of materials simultaneously [35]. The presence of SRO in CoCrNi could elevate the activation potential that modulates dislocation activity, thereby influence the selection of dislocation paths during the slip, fracture, and twinning processes [28]. A more recent study by Chen *et al.* further put forward the proposition that SRO can effectively enhance both the plasticity and strength of CoCuFeNiPd HEA [36]. These findings open up new avenues for investigating the potential benefits of SRO in improving the mechanical performance of HEAs.

In this regard of the effect of SRO on mechanical behavior, Antillon *et al.* investigated the SRO strengthening in FCC and BCC quaternary Co-Fe-Ni-Ti HEAs, respectively [25,28]. They evaluated the effect of solid-solution strengthening by calculating the energy topology of dislocations moving through the complex atomic environment. Research results show that the interplay between misfit components and chemical SRO has an effect on the overall critical resolved shear stress for FCC  $\text{Co}_{30}\text{Fe}_{16.66}\text{Ni}_{36.67}\text{Ti}_{16.67}$  [28]. The role of SRO on critical yield stress is quantified and compared with the current solid-solution models for FCC and BCC CoFeNiTi [25,28]. Whereas the understanding of SRO effects on other mechanical properties, such as the intrinsic deformation mechanism involved in single crystalline and polycrystalline  $\text{Co}_{30}\text{Fe}_{16.66}\text{Ni}_{36.67}\text{Ti}_{16.67}$  HEAs, is still limited. So, the further research is warranted to elucidate the role of SRO in the physical properties for  $\text{Co}_{30}\text{Fe}_{16.66}\text{Ni}_{36.67}\text{Ti}_{16.67}$ , specifically the temperature dependent SRO parameter, the degree of serve LLD, GSFE, and connecting to the mechanical properties, such as tensile and shear deformation mechanism.

Due to the atomic-level nature of SRO, its experimental observation may present challenges. Herein the atomistic simulations have emerged as a powerful approach to investigating SRO. Based on the searching mechanism from Monte-Carlo (MC) method, ones often combine the classical molecular dynamics (MD), density functional theory (DFT), cluster expansion (CE), or Landau-type theory method to predict the SRO [7,15,20,37–40] in HEAs. For instance, Jian *et al.* employed the hybrid MC/MD simulated method to explore the effects of lattice distortion and SRO on the formation and evolution of dislocation in CoCrNi [13,20,41]. With the similar method, the mechanism of phase transformation from FCC to BCC was studied for Co-Fe-Ni-Ti HEAs [25,26]. Zhu *et al.* used the hybrid MC/DFT method to calculate the effect of SRO on GSFE for equiatomic FCC CoCrNi, CoNiV and CoCrFeMnNi. They explored the physical origin of different deformation mechanisms of three alloys [15]. By using the combination of CE and MC methods, the Mn-Ni SRO significantly increases the temperature of order-disorder transformation in the vicinity of L10-MnNi and to the equiatomic region of FCC Cr-Fe-Mn-Ni HEAs [7]. In additions, the Korringa-Kohn-Rostoker (KKR) Green's-function electronic-structure method in combination with the inhomogeneous coherent-potential approximation (CPA) was also used to predict all pair correlations and interpret the Warren-Cowley SRO parameter [42]. Based on the available order structures

(for instance, L11 and L12) in FCC lattice matrix, the *ab initio* calculated Gibbs free energy could help to predict the SRO in FCC 3d HEAs [43].

In this work, based on the hybrid MC/MD, we discuss the SRO role in FCC  $\text{Co}_{30}\text{Fe}_{16.66}\text{Ni}_{36.67}\text{Ti}_{16.67}$  HEA by using the pairwise multicomponent order parameter. We adopt the atomic displacement apart from ideal lattice sites, atomic pair difference, and Voronoi tessellation to comprehensively discuss the SRO and temperature dependent lattice distortion, due to the less severe LLD in FCC HEAs. The GSFE as a function of temperature shows an interesting increase. Further we in detail investigate the influence of SRO on tensile and shear strength of single crystalline and polycrystalline Co-Fe-Ni-Ti HEA.

The rest of the paper is organized as follows. In Sec. II, we present the theoretical tool and give the important details of simulation. The results are presented and discussed in Sec. III, including SRO and its effect on LLD, GSFE, and tensile and shear mechanical behaviors. The paper ends with conclusions.

## II. MODELING AND METHODS

In the present work, all simulations were carried out by using the Large scale molecular dynamics parallel simulator (LAMMPS) [28]. The accuracy of MD simulations depends heavily on the interatomic potentials between metallic elements. We used the embedded atom method (EAM) potentials developed by Zhou *et al.* [23], which have been validated by researchers and applied in the related studies on the FCC and BCC Co-Fe-Ni-Ti alloys [20,26,28,41]. The structural model was visualized in the open source visualization software (OVITO). The crystal structure extraction and dislocation analysis were achieved by the common neighbor analysis (CNA) and dislocation analysis (DXA) functions [44].

To investigate the structural properties of FCC  $\text{Co}_{30}\text{Fe}_{16.66}\text{Ni}_{36.67}\text{Ti}_{16.67}$  HEA with the chemical disorder, we utilized the ATOMSK software [45] to establish an FCC supercell containing 72 000 atoms ( $20 \times 30 \times 20$ ) as the initial configuration. This supercell was oriented along the  $X$ ,  $Y$ , and  $Z$  axes, corresponding to the  $\langle 11\bar{2} \rangle$ ,  $\langle 111 \rangle$ , and  $\langle \bar{1}10 \rangle$  crystalline directions, respectively. The random distribution of metallic elements was achieved using the similar atomic environment (SAE) method [16,46]. The periodic boundary condition was applied along all three coordinate axes. We determined the lattice constant  $a_0$  by calculating the total energy while keeping the lattice parameter fixed within the FCC crystal structure, varying it from 3.4 to 3.8 Å for our initial configuration. The curve with the lowest total energy is shown in Fig. S1 (see Ref. [47]). The lattice constant is found to be  $a_0 = 3.630$  Å at 0 K. We estimated the lattice constants for temperatures in the range of 300–1100 K by allowing the structure to relax within the NPT ensemble (constant number of atoms, constant pressure, and constant temperature).

The chemical SRO structure was predicted using the hybrid Monte Carlo/Molecular Dynamics (MC/MD) method. Initially, the configuration is relaxed for 1000 picoseconds (ps) within the NPT ensemble, enabling the atoms to achieve full mobility. This relaxation process ensures a more reasonable distribution of atomic positions and brings the configuration to the desired annealing temperature. Subsequently, the random

TABLE I. Elastic constants  $C_{ij}$  (in unit of GPa) and Debye temperature  $\Theta_D$  (in unit of K) of SRO and RSS structures for FCC Co-Fe-Ni-Ti HEA at different temperatures.

Parameter	Model	300 K	500 K	700 K	900 K	1100 K
$C_{11}$	RSS	143.90	136.86	129.75	124.61	117.84
	SRO	150.88	140.47	133.66	126.04	120.82
$C_{12}$	RSS	114.15	110.59	106.97	104.34	100.92
	SRO	115.44	109.79	108.51	104.12	101.08
$C_{44}$	RSS	68.47	65.04	61.31	56.67	54.45
	SRO	70.97	67.47	63.71	57.68	55.74
$\Theta_D$	RSS	364.32	351.23	336.96	322.42	309.76
	SRO	380.10	364.98	346.92	328.52	320.03

exchange of different atomic pairs is performed using the MC exchange method. The temperature is maintained at a specific annealing temperature, and the kinetic energy of each atom remains constant after the exchange. The structural optimization in MD simulations is conducted after every 100 MC exchanges. This combination of MC steps and MD relaxation processes is extremely effective in achieving the convergence of the equilibrium positions and the corresponding atomic displacements. The acceptance of each MC atom exchange is determined by the Metropolis criterion [48], which could evaluate whether  $\theta < \frac{P_{\text{final}}}{P_{\text{initial}}}$ . Here,  $\theta$  is a random number within the range  $[0, 1]$ ,  $P_i$  represents the Boltzmann distribution function ( $P_i = e^{-\beta U_i}$ ),  $\beta = \frac{1}{k_B T}$ , and  $U_i$  signifies the potential energy of the system. To assess the energy convergence during annealing at different temperatures, the curve of potential energy as a function of the number of atomic exchanges is presented in Fig. S2 [47]. The potential energy exhibits convergence after 250 000 cycles, with a decrease of approximately 0.015 eV per atom.

At finite temperature, the thermal vibration induced atomic displacement apart from ideal lattice site  $\Delta d_{\text{TV}}$  could be estimated by the harmonic Debye model [49], which is defined as

$$\Delta d_{\text{TV}} \approx \sqrt{\frac{9\hbar^2 T^2}{M k_B \Theta_D^3} \int_0^{\Theta_D/T} \frac{x}{e^x - 1} dx}, \quad (1)$$

where  $T$  stands for the finite temperature,  $\hbar = h/2\pi$  for the reduced Planck constant,  $M$  for the atomic mass, and  $k_B$  for the Boltzmann constant.  $\Theta_D$  is the Debye temperature. Note that the correction for zero-point energy derived from the quantum effect is ignored in Eq. (1). Here, we calculate the elastic constants at finite temperature to obtain the sound velocity, further estimate the Debye temperature. For the temperature dependent elastic constants, we used the stress-strain method in combination with MD simulation to calculate the elastic constants of RSS and SRO structures at different temperatures. Both the elastic constants and Debye temperature are listed in Table I. The elastic constants regularly soften as the temperature rises. The SRO has a minor influence on the elastic constants and Debye temperature. These results are consistent with the other reports [50,51]. It suggests that the present calculations are reasonable.

MD simulations were consistently applied for all constructed configurations to discuss the temperature dependent

GSFE in SRO and RSS structures and to enable the comparative analysis of mechanical properties including tensile and shear deformation results for both single crystalline and polycrystalline Co-Fe-Ni-Ti HEA. The tensile deformation configuration composed of 576 000 atoms was expanded from the initial model by introducing  $2 \times 2 \times 2$  unit cells along the  $X$ ,  $Y$ , and  $Z$  axes. To attain the equilibrium structure, the tensile configurations undergo the relaxation within NPT ensemble at 300 K, followed by further relaxation within the NVT ensemble (constant number of atoms, constant volume, constant temperature) at the same energy level of 300 K.

The tensile deformation is loaded along the  $Z$  axis ( $\langle \bar{1}10 \rangle$  crystal direction). The simulations run for 200 ps to achieve a total strain of 20%, with an engineering strain rate of  $1.0 \times 10^{-3}$  at 300 K and atmospheric pressure. In the case of shear deformation configurations, we constructed an initial model consisting of a  $3 \times 3 \times 3$  unit cell with a total of 1 944 000 atoms. The  $X$ ,  $Y$ , and  $Z$  directions were defined as  $\langle 112 \rangle$ ,  $\langle \bar{1}\bar{1}1 \rangle$  and  $\langle 1\bar{1}0 \rangle$ , respectively. The shear deformation is applied to the  $\langle \bar{1}\bar{1}1 \rangle$  plane along  $\langle 112 \rangle$  under the NPT ensemble, with the shear strain rate of  $1.0 \times 10^{-3}$ . The simulations ran for a total of 300 ps to achieve the 30% strain.

### III. RESULTS AND DISCUSSION

#### A. Short-range order (SRO) parameters

For the multicomponent SRO in high-order system, Ceguerra *et al.* proposed the generalized theory by using two sets of atomic species or by containing pair-atom and three-atom clusters [46,52,53]. According to De Fontaine's model, the pairwise multicomponent short-range order (PM-SRO) parameter is defined as

$$\alpha_{\text{AB}}^m = \frac{p_{\text{AB}}^m - c_{\text{B}}}{\delta_{\text{AB}} - c_{\text{B}}}, \quad (2)$$

where  $\delta_{\text{AB}}$  is equal to one if  $A=B$  and zero otherwise, and  $p_{\text{AB}}^m$  is the average probability of finding a B-type atom in the  $m$ th shell around a A-type atom.  $c_{\text{B}}$  is the concentration of B atom in alloys. Due to the examination of pairs of atomic species, this parameter is pertinent for multicomponent systems containing ternary or higher order alloys. For binary alloys, it could turn into the WC-SRO parameter [52,54]

$$\alpha_{\text{AB}}^m = 1 - \frac{p_{\text{AB}}^m}{c_{\text{B}}}, \quad (3)$$

$\alpha_{\text{AB}}^m = 0$  is for the random solid solution. When  $\alpha_{\text{AB}}^m > 0$ , there is the segregation of A-B atomic pairs, meaning that the number of A-B atomic pairs is less than that of random case. Whereas  $\alpha_{\text{AB}}^m < 0$  is corresponding to the SRO in the A-B atomic pairs, indicating an increase in the number of the nearest neighbors in the A-B type atomic pairs. In the present work, we only consider the first nearest neighboring (1NN) shell layer, i.e.,  $m = 1$  in SRO parameters.

For the atomic distribution in the random and PM-SRO solid solutions for Co-Fe-Ni-Ti HEA, we show the PM-SRO parameters of 10 different atomic pairs in Fig. 1. All atomic pairs have  $\alpha_{\text{AB}} \approx 0$  for RSS, indicating that the initial (72 000 atoms) configuration satisfies the random solid solution. It is well known that the MC temperature is not physical quantity.

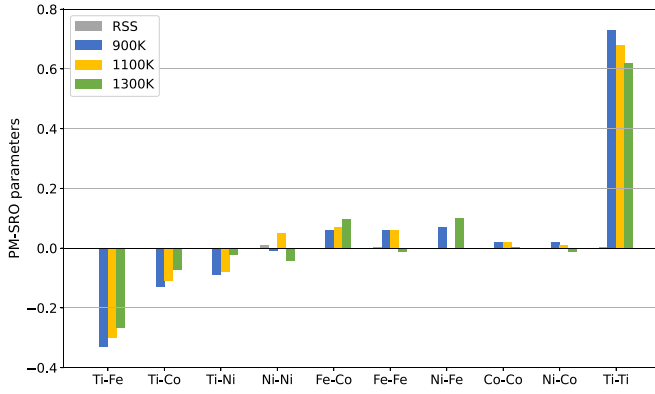


FIG. 1. The pairwise multicomponent short-range order (PM-SRO) parameters in FCC Co-Fe-Ni-Ti HEA at different simulated annealing temperatures and random solid solution (RSS).

Whereas the simulation data at different MC temperatures suggest the likeliness of the predicted PM-SRO, because the local energy barrier for site swaps is overcome by tuning the MC temperature. From the overall perspective of PM-SRO at three temperatures, the absolute values of SRO parameters gradually decrease with the increase of annealing temperature. It indicates that the alloy tends to a disordered state in the high-temperature system without obvious element segregation.

With the decrease of simulated annealing temperature, the PM-SRO parameters become negative or positive for Ti- $X$  ( $X = \text{Ti, Fe, Ni, Co}$ ) atomic pairs, the negative PM-SRO suggest that the Ni, Co, and Fe prefer to occupy near Ti atoms, Ti and Fe atoms could be easy to form clusters. While the positive PM-SRO magnitude hints that the strong repulsion and the tendency of cosegregation occur between Ti atoms. This could be explained by the electronegativity difference between atoms and the first-neighbor solid solution interaction energies [55]. For example the close electronegativity value is 1.88 for Co, 1.91 for Ni, and 1.83 for Fe, whereas this value is only 1.54 for Ti. From Fig. 1, we could see the small positive PM-SRO parameters for Fe-Fe, Fe-Co, and Fe-Ni atomic pairs, but the near zero or even slightly negative PM-SRO parameters for Co-Co, Co-Ni, and Ni-Ni atomic pairs under the present annealing temperatures. The prediction is in agreement with the existing SRO between the early and last  $3d$  transition metallic atoms in CoCrNi, CoCrFeNi, CoFeNiV, and CoCrFeMnNi HEAs [11,15,46,56].

### B. Effect of SRO on the lattice distortion

Due to the local atomic arrangements affected by the local stress distribution, bonding energy, and electronic and magnetic coupling [57], HEAs exhibit the varying degrees of intrinsic lattice distortion, which depends on the metallic elements and composition of alloys. The constituent hyperspace of HEAs provides high degrees of freedom to adjust the lattice distortion and to have important effect on the phase stability, further tune the mechanical behaviors. Owen *et al.*

well defined three types of lattice distortion [18] and reviewed the lattice distortion in HEAs [17,18,58].

One of the most intuitive description on LLD is the atomic size difference. Based on the atomic radii data from the measurement of x-ray diffraction in their elemental states or the 12-coordinated system, the atomic size mismatch ( $\delta$ ) was frequently adopted to measure the lattice distortion in HEAs. The  $\delta = 11.2\%$  in of Co-Fe-Ni-Ti HEA is larger than the indicator  $\delta = 8.5\%$  of simple phase HEAs [59,60]. According to this classical definition, if the atomic radii was accurate enough, the degree of lattice distortion could be well understood by using the atomic radius mismatch. When the effect of local atomic environment (such as SRO) and temperature on the lattice distortion is considered, the lattice distortion could be required to describe by using the atomic displacement away from ideal lattice site [16], atomic pair difference [61], and atomic volume difference [56] in the atomistic simulations.

#### 1. Atomic displacement away from ideal lattice sites

HEAs are solid solutions with crystalline structures. The important assumption on the atoms occupying the ideal lattice sites is often used to understand the related structural properties. Whereas the fact is that the metallic atoms deviate from their ideal lattice positions due to the stacking of different-size atoms and thermal vibration. Here we define the lattice distortion as the degree of atomic displacement apart from the ideal lattice site of of metallic atoms,

$$\begin{aligned} \Delta d_{LD} &= \Delta d - \Delta d_{TV} \\ &= \frac{1}{N_a} \sum_i \sqrt{(x_i - x'_i)^2 + (y_i - y'_i)^2 + (z_i - z'_i)^2} \\ &\quad - \Delta d_{TV}, \end{aligned} \quad (4)$$

where  $N_a$  is the total number of atoms, the symbols  $x_i$  ( $x'_i$ ),  $y_i$  ( $y'_i$ ), and  $z_i$  ( $z'_i$ ) are the atomic coordinates after (before) lattice distortion. Combining Eq. (1) with Eq. (4), we could obtain the lattice distortion  $\Delta d_{LD}$  derived from different atomic sizes at finite temperature, via the combination of the MD simulation and Debye model.

Figure 2 shows the atomic displacement away from ideal lattice sites  $\Delta d$  of random and SRO solid solution for  $\text{Co}_{30}\text{Fe}_{16.66}\text{Ni}_{36.67}\text{Ti}_{16.67}$  at finite temperature. At 0 K temperature the present HEA keeps a small lattice distortion of  $\Delta d = 0.054 \text{ \AA}$ , the relative difference is 1.48%, which is consistent with the *ab initio* calculations of FCC HEAs [16]. The degree of  $\Delta d$  quickly increases as the temperature rises. The  $\Delta d$  increases up to  $0.6433 \text{ \AA}$  for RSS  $\text{Co}_{30}\text{Fe}_{16.66}\text{Ni}_{36.67}\text{Ti}_{16.67}$  at 1100 K. From Fig. 2, we could see that SRO does not significantly reduce  $\Delta d$ . The  $\Delta d$  as a function of temperature could be described as a linear relation ( $\Delta d = a \times T + b$ ) from 300 to 1100 K. It is interesting that each metallic element has the similar slope [ $a = (0.54-0.55) \times 10^{-4}$ ] and the intercept  $b$  represents the intrinsic LLD of metallic element at 0 K, as shown in Fig. S3 [47]. Ti has the severest LLD, followed by Co, while Fe and Ni have the close LLD degree. As the lightest element in Co-Fe-Ni-Ti HEA, Ti atoms tend to adjust these differences through atomic displacement to stabilize the structure.

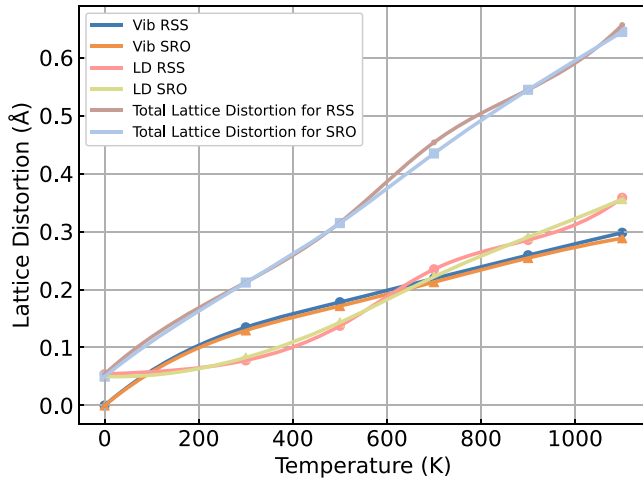


FIG. 2. The atomic displacement apart from ideal lattice site ( $\Delta d$ ), the lattice distortion from atomic size difference ( $\Delta d_{LD}$ ), and the thermal vibration induced atomic displacement ( $\Delta d_{TV}$ ) for RSS and SRO configurations at different temperatures.

In order to study the lattice distortion from atomic size difference  $\Delta d_{LD}$ , we estimate the thermal vibration induced atomic displacement  $\Delta d_{TV}$  by using the Deybe model [Eq. (1)].  $\Delta d_{TV}$  shows a nonlinear increase as the temperature rises. Without the influence of zero-point vibration,  $\Delta d_{LD}$  surpasses  $\Delta d_{TV}$  at low temperature (0–100 K). As the temperature rises, the lattice thermal vibration induces a notable increase of  $\Delta d_{TV}$ . However, the rate of increase of  $\Delta d_{TV}$  trends to the constant. Instead the severe degree of  $\Delta d_{LD}$  slowly increases, then quickly increases with the rising temperature. It results in the large  $\Delta d_{TV}$  compared to  $\Delta d_{LD}$  below 600 K and the crossing among  $\Delta d_{LD}$  and  $\Delta d_{TV}$  near 600 K. Whereas the  $\Delta d_{LD}$  becomes larger than  $\Delta d_{TV}$  above 600 K, due to the quick increase of lattice distortion derived from positive lattice thermal expansion. Interestingly, for CoCr-FeMnNi, the LD degree keeps a constant after considering the Debye model based thermal vibration induced atomic displacement [62]. We note that the mean-field representation on interatomic potential [55] has been used to estimate the thermal vibration induced atomic deviation via the full width at half maximum (FWHM) of radial distribution function. Using this way, Jian *et al.* found that the degree of LD decrease with increases of temperature, when the thermal vibrations increase [41].

The emergence of SRO is anticipated to tune the lattice distortion, enhance the ductility of HEAs, and improve the superelastic properties of HEAs [40,41,63]. However, from Fig. 2, we could find that 1NN SRO do not have an important effect on the atomic displacement apart from ideal lattice site  $\Delta d$  and  $\Delta d_{TV}$ , further  $\Delta d_{LD}$  do not have important decrease due to SRO. It is necessary to note that 1NN SRO is only considered in our calculations.

## 2. Difference of atomic pairs

As discussed in recent work by Tan *et al.* [61,64], it is not easy to interpret the mechanism of LLD due to the difficulties in accurate estimation of atomic size in the fact atomic

TABLE II. Local lattice distortion of the first nearest neighboring  $i$ - $j$  atoms pair for RSS and SRO Co-Fe-Ni-Ti HEA at 300–1100 K.

$\chi_i$	Model	300 K	500 K	700 K	900 K	1100 K
Co-center	RSS	3.52%	4.27%	4.59%	4.8%	5.18%
	SRO	3.71%	4.06%	4.34%	4.58%	4.84%
Fe-center	RSS	3.70%	4.44%	4.7%	4.99%	5.31%
	SRO	3.36%	3.87%	4.13%	4.48%	4.76%
Ni-center	RSS	3.584%	4.33%	4.65%	4.92%	5.24%
	SRO	3.71%	4.18%	4.44%	4.70%	4.94%
Ti-center	RSS	2.465%	2.69%	2.87%	3.0%	3.25%
	SRO	2.28%	2.53%	2.84%	3.16%	3.38%

environment. Here we employ the length of atomic pair to quantify the LLD. The difference of atomic pairs is defined as

$$\chi_i = \sqrt{\frac{1}{N} \sum_j^n \sum_{N=1}^{N_{ij}} \left(1 - \frac{r_{i-j}}{\bar{r}}\right)^2}, \quad (5)$$

where  $\chi_i$  stands for the degree of LLD at the center of  $i$  metallic element.  $\bar{r}$  is the 1NN interatomic distance of the crystal structure,  $\bar{r} = \frac{\sqrt{2}a_0}{2}$ ,  $a_0$  is the lattice parameter.  $N$  is the number of first nearest neighbor atoms of center atom  $i$  in statistics.  $\sum_j^n$  represents the summary of all 1NN atomic pairs, without distinguishing the types of metallic elements. Because the atoms have an uncertain displacement derived from the lattice thermal vibration and lattice distortion, the atoms are disturbed near the equilibrium lattice sites. The distance between  $i$ - $j$  atomic pairs  $r_{ij}$  could be calculated through atomic coordinates. The number of 1NN atoms  $j$  is determined by the radial distribution function.

Table II lists the 1NN LLD at finite temperature ranging from 300 to 1100 K. We found that the LLD of metallic atoms also increases significantly with rising temperature and is between 2.465%–5.31% for RSS and 2.28%–4.94% for SRO. The increase of LLD degree is suppressed, but the influence of SRO on LLD is relatively small, which is consistent with the displacement of an atom away from its ideal lattice position. From Fig. 2, the lattice distortion in the 1NN SRO configuration is less than or equal to the LD in the RSS structure. The LLD in SRO is smaller of 0.06% than the  $\chi_i$  of RSS, except for the LLD for Ni and Co at 300 K, which are slightly larger than the LLD in RSS configuration. In some HEAs, such as the Co-Ni-Ti-Zr-Hf-Fe Elinvar alloy, as emphasized in reference [65,66], it has been experimentally demonstrated that the formation of SRO could reduce the lattice distortion. The degree of LLD at the center of Ti atoms is relatively small, due to the strong bonding and large charge transfer between Ti-X ( $X = \text{Co, Fe, Ni}$ ) atomic pairs. While the similar bonding behaviors and electronegativity of Fe, Ni and Co make their LLD very close and severe. The large charge transfer or electronegativity difference could result in the reduced size mismatch between the elements. The similar case occurs in the HfNbTiVZr refractory alloys [67].

$$\chi_{i-j} = \sqrt{\frac{1}{N_{ij}} \sum_{N=1}^{N_{ij}} \left(1 - \frac{r_{i-j}}{\bar{r}}\right)^2} \quad (6)$$

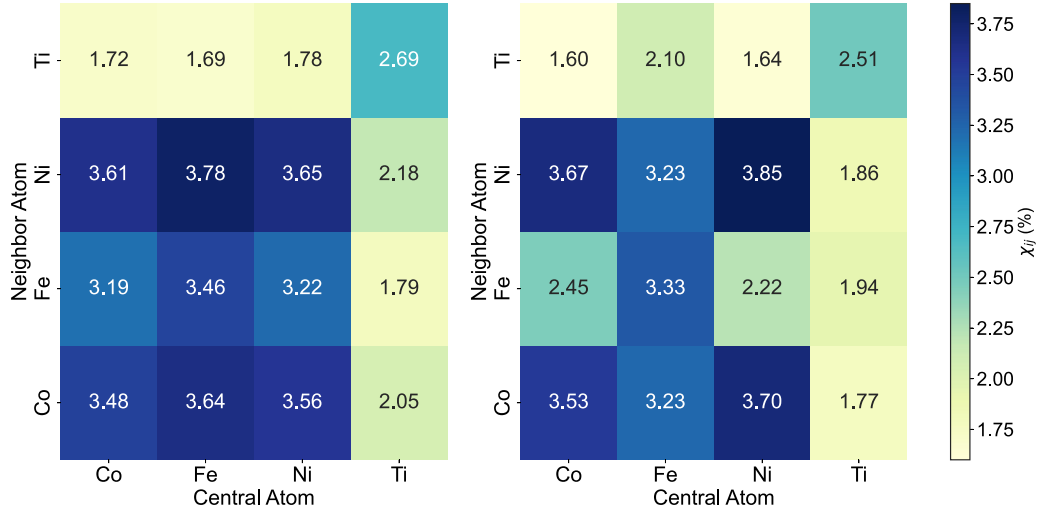


FIG. 3. The degree of local lattice distortion ( $\chi_{i-j}$ ) of 1NN atomic pair  $i - j$  for RSS (left) and SRO (right) Co-Fe-Ni-Ti HEA at 300 K.

Equation (5) describes the offset length of atomic pairs in the distorted configurations, and could only be used to study the lattice distortion between the same atom and the whole crystal environment. In order to distinguish the LLD degree of the 1NN atoms and investigate the impact of SRO on the local atomic environment, we introduce Eq. (6) to calculate the LLD of 1NN atoms,  $\chi_{i-j}$ . Recently, researchers have used Eq. (6) to estimate quantitatively the LLD via the combination of the high resolution transmission electron microscope (HRTEM) and extended x-ray absorption fine structure spectrum (EXAFS) [61,64].

Figure 3 shows the LLD of 1NN atomic pair  $i - j$  at the reference center element  $j$ . The degree of LLD strongly depend on the local environment of reference center atoms, for example, the typical Ti-Fe atomic pair,  $\chi_{\text{Ti-Fe}} = 1.69$  is different from  $\chi_{\text{Fe-Ti}} = 1.94$  for RSS configuration, whereas in the SRO configurations  $\chi_{\text{Ti-Fe}} = 2.10$  is slightly close to  $\chi_{\text{Fe-Ti}} = 1.94$ . The comparison of left and right panels in Fig. 3 indicates that SRO has an important effect on the degree of LLD  $\chi_{\text{Fe-X}}$  for 1NN atomic pairs Fe-X ( $X = \text{Co, Fe, Ni, Ti}$ ). For instance, the degree of LLD of Fe-X at the central atom Co, Fe, Ni and Ti is 3.19, 3.45, 3.22, and 1.78 in the RSS structure, respectively, whereas the value is 2.45, 3.33, 2.22, and 1.94 in SRO. The change of LLD degree  $\chi_{\text{Ti-X}}$  of 1NN atomic pairs Ti-X ( $X = \text{Co, Fe, Ni, Ti}$ ) at the central atom Co/Fe/Ni/Ti is very small between RSS and SRO structures. It is consistent with the  $\chi_{\text{Ti}}$  values (see Table II). The positive SRO parameters between Fe and Fe, Co, and Ni atomic pairs suggest that the 1NN atoms at the Fe center appear the obvious segregation and produce the severe lattice distortion around the Fe atom. Although Ti-Ti atomic pair has more positive SRO parameter, the strong bonding between Ti-X ( $X = \text{Fe, Ni, Co}$ ) hinders the random distribution of Ti atoms and reduces the number of 1NN Ti atoms at the central element Ti. This further reduces the LLD degree of Ti-Ti atomic pair. Interestingly, SRO increases the LLD degree  $\chi_{\text{Ni-Ni}}$  from 3.65 to 3.85 for the Ni-Fe atomic pair at the reference atom Fe. These results indicate that the positional and dynamical behavior of the Co-Fe-Ni-Ti HEA is complex and not captured by the simple statistical models applied here.

### 3. Voronoi tessellation

Similar to the difference of atomic pairs, the Voronoi tessellation is also geometry-based analysis and not rooted in physical properties of materials. However, it is a useful approach to facilitate the analysis of local atomic structure. Thus we calculated the Voronoi volume of each atom in the defect-free bulk supercell to elucidate the correlation between chemical SRO and LLD via the average Voronoi volume and volumetric distribution of each metallic element.

Table III shows that the average Voronoi volume of each metallic element at finite temperature (300-700 K). In the RSS configuration, the voronio volume of each metallic element increases as the temperature rises. The close average volume is for Co, Ni and Fe atoms, while Ti atoms have the largest average volume. In the case of SRO structure, the average Voronoi volume of Ni, Fe and Ti atoms reduce first and then increase, but the average volumes of Ni and Fe atoms become extremely different. The average volume of Co atoms enlarges with increasing temperature. From Table III, we could see that the average Voronoi volume of Fe in SRO configuration is larger than that in RSS structure at 300 K and 700 K, but SRO induces the large decrease of average volume of Ti and Ni at 500 K. The Co atoms have close average volume in RSS and SRO configurations at the present range of temperature. These

TABLE III. Average Voronoi volume for each metallic element at 300, 500, and 700 K. The unit is  $\text{\AA}^3$ .

Element	Model	300 K	500 K	700 K
Co	RSS	12.098	12.214	12.339
	SRO	12.035	12.220	12.341
Fe	RSS	12.096	12.219	12.350
	SRO	12.546	12.090	12.523
Ni	RSS	12.090	12.207	12.339
	SRO	11.932	11.873	12.325
Ti	RSS	13.046	13.172	13.334
	SRO	12.952	12.518	12.982

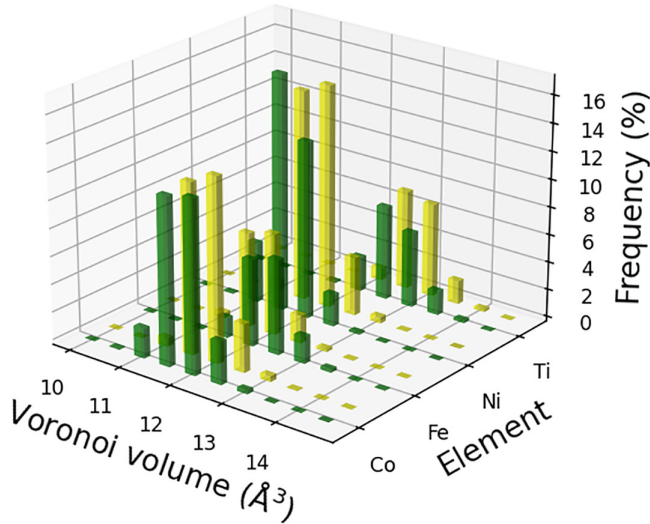


FIG. 4. Voronoi volume distribution of each metallic element in 32 000-atom SRO (green) and RSS (yellow) configurations at 300 K.

findings suggest that the SRO could induce the complicated chemical composition fluctuation.

Figure 4 shows the normal distribution of Voronoi volume of metallic atoms in SRO and RSS configurations at 300 K. The similar distribution of volume for Co atoms further suggest the close average volume exists in RSS and SRO configurations. From Fig. 4, we can see that SRO makes Fe atoms significantly expand their volume by referencing the volume of Co and Ni atoms. However, the average Voronoi volume of Ti and Ni in SRO is slightly smaller than that of RSS. This is due to the clear SRO around the Ti metallic atoms. The strong SRO of Fe and Ti atoms indicates that Fe and Ti atoms are biased together. Comparing with the distribution of volume in RSS, Fe, Ni, and Ti metallic atoms expand their domain. So the 1NN SRO plays an important role in the Voronoi volume and the local atomic environment.

### C. Effect of SRO on the generalized stacking fault energy

The generalized stacking fault energy (GSFE) is a valuable parameter for comprehending the deformation behavior of HEAs. However, the experimental measurements provide only stable stacking fault energy, such as the intrinsic stacking energy  $\gamma_{\text{isf}}$ . Fortunately, the atomistic simulations could reveal the GSFE, including the unstable stacking fault energy  $\gamma_{\text{usf}}$ , and extrinsic stacking faults  $\gamma_{\text{utf}}$ , and twinning stacking fault energy  $\gamma_{\text{twf}}$ , as a function of displacement of incomplete dislocation. Because of the complicated composition, the existence of SRO, and fluctuations of the composition proportions within each atomic layer are inevitable in HEAs. This leads to the strong dependence of GSFE on the specific stacking fault planes, making GSFE calculations on HEAs less representative compared to the traditional elemental metals.

To mitigate the impact of composition fluctuations on GSFE calculations, the large-scale atomistic simulations are necessary. We construct the large configurations consisting of 134,400 atoms, aligned with the crystal directions  $[11\bar{2}]$ ,  $[111]$ , and  $[1\bar{1}0]$ , and with the stacking surface area of 162 nm<sup>2</sup>. Our structures satisfy the condition of periodic boundary. By rigidly shifting the upper block along the  $[11\bar{2}]$  direction within the (111) plane while keeping the lower block fixed, we could calculate the energy change for the entire simulation configuration. This allows us to determine the GSFE as a function of displacement using the definition

$$\gamma = \frac{1}{A}(E_f - E_0), \quad (7)$$

where  $E_0$  is the initial energy of perfect configuration,  $E_f$  is the energy of configuration with the layer stacking faults,  $A$  is the area of the slip plane. In Fig. 5, we show three scenarios in the process of stacking faults: one without slip, another with slip along  $[11\bar{2}]$  at a displacement of  $1.0b_p$ , ( $b_p = a_0/6(11\bar{2})$ ), and the final snapshot with slip at the position corresponding to  $2.0b_p$ . Here,  $a_0$  represents the lattice parameter of the unit cell.

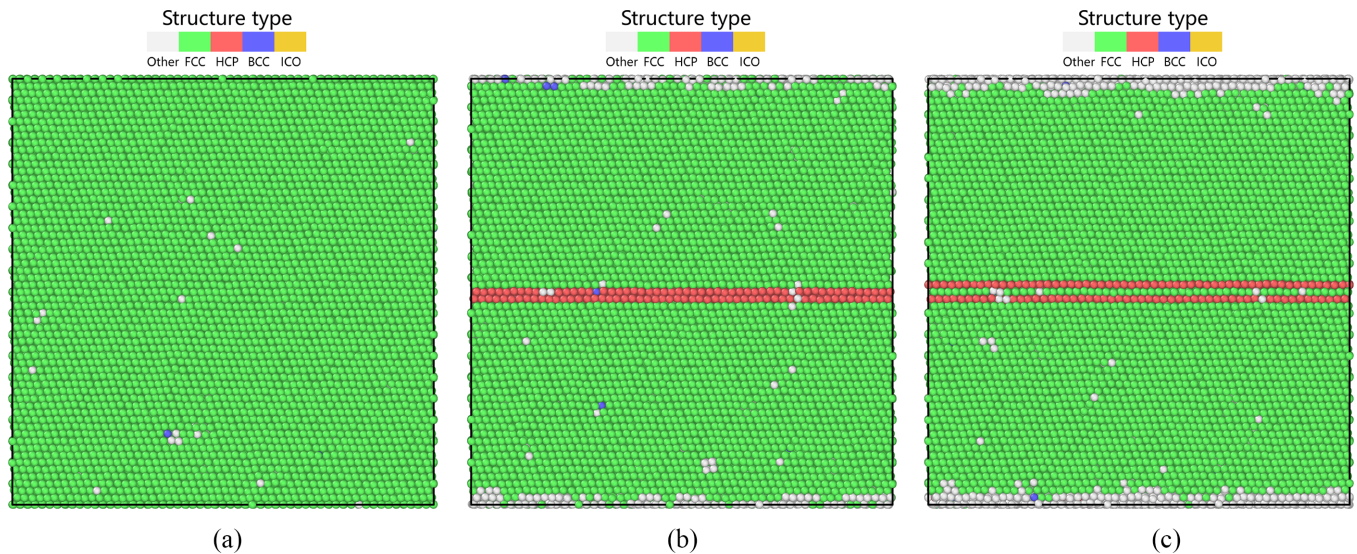


FIG. 5. Shown are the snapshots of the configuration without slip (a), with the intrinsic stacking faults (b), and with the extrinsic stacking faults (c).

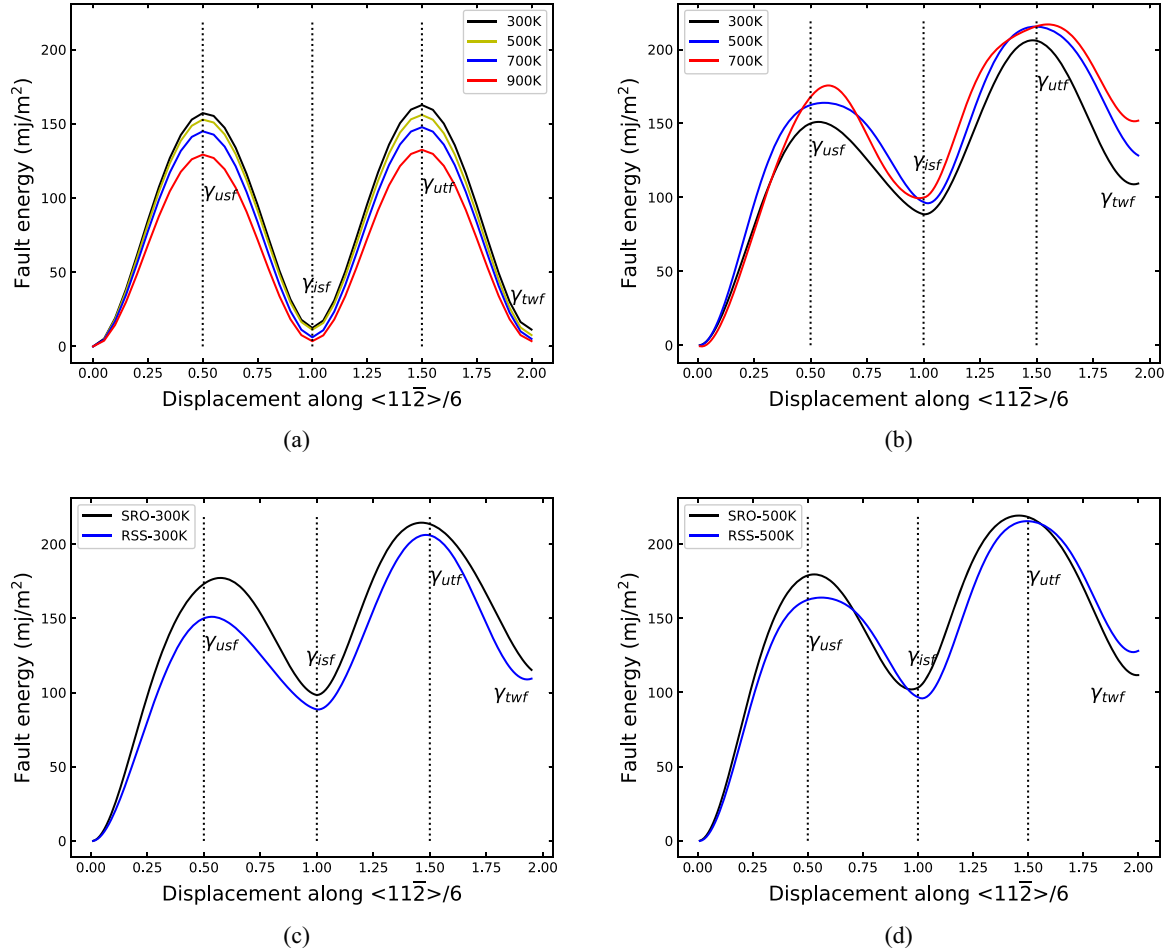


FIG. 6. Shown are the GSF E curves calculated by the quasistatic approximation at different temperatures (a), the GSF E curves calculated by MD at different temperatures (b), and the GSF E curves for SRO configuration at 500 and 700 K [(c) and (d)].

Taking into account the crystal thermal expansion effect, we employ the quasistatic approximation to calculate the GSF E of the RSS Co-Fe-Ni-Ti HEA at finite temperature. Figure 6(a) suggests that  $\gamma_{\text{isf}}$  is less sensitive to temperature, consistently maintaining a value below 20 mJ/m<sup>2</sup>, compared to  $\gamma_{\text{usf}}$  and  $\gamma_{\text{utf}}$ . This observation aligns with the results reported by Jian *et al.* [41]. The GSF E decreases with increasing temperature and lattice constant, mirroring the predicted trend of pure metals when the density functional theory (DFT) is used to account for temperature effects [68]. In DFT calculations, the free energy encompasses the electronic, harmonic vibrational, magnetic, explicit anharmonic contributions, and their coupling term. Note that the free energy calculation is based on the ideal lattice site, due to pure metal. In our quasistatic simulation, we omit of the lattice distortion, lattice vibrations and other structural aspects during dislocation slipping, such as the presence of SRO and the formation of other phases (e.g., BCC, HCP, and unknown phases) during the stretching process. To address these effects comprehensively, we conducted the molecular dynamics simulations of GSF E in the NVT ensemble. Figure 6(b) illustrates an anomalous increase in GSF E with rising temperature. The appearance of typical stacking fault energies is apart from the ideal displacement of incomplete dislocations as the temperature rises. These findings are primarily attributed to the composition

fluctuations, lattice distortion, and local phase transitions, in contrast to the more conventional mechanism of lattice volumetric expansion [14]. Intriguingly, this anomalous behavior has also been observed in the FCC alloys, for instance, CoNi and CoCrNi [69,70].

Figures 6(c) and 6(d) unveil that SRO could significantly influence the GSF E of Co-Fe-Ni-Ti HEA. At 500 K, when the displacement of incomplete dislocations locates near 0.75  $b_p$  and between 1.60–2.00  $b_p$ , the SRO induces the lower SFE, compared to RSS. Table IV quantifies the typical SFE difference between RSS and SRO configurations. The influence of SRO on  $\gamma_{\text{isf}}$  is notably substantial. At 300 K, SRO elevates  $\gamma_{\text{usf}}$  by 24 mJ/m<sup>2</sup> and  $\gamma_{\text{isf}}$  by 11 mJ/m<sup>2</sup>, while  $\gamma_{\text{utf}}$  experiences a more modest increase of 9 mJ/m<sup>2</sup>. At 500 K, these values become small and even negative, for instance,  $\gamma_{\text{twf}}^{\text{SRO}} - \gamma_{\text{twf}}^{\text{RSS}} = -16$  mJ/m<sup>2</sup>.

TABLE IV. The effect of SRO on typical stacking fault energies ( $\gamma_{\text{usf}}$ ,  $\gamma_{\text{isf}}$ ,  $\gamma_{\text{utf}}$ , and  $\gamma_{\text{twf}}$  in unit of mJ/m<sup>2</sup>) of HEAs at temperature  $T = 300$  and 500 K.

$T$	$\gamma_{\text{usf}}^{\text{SRO}} - \gamma_{\text{usf}}^{\text{RSS}}$	$\gamma_{\text{isf}}^{\text{SRO}} - \gamma_{\text{isf}}^{\text{RSS}}$	$\gamma_{\text{utf}}^{\text{SRO}} - \gamma_{\text{utf}}^{\text{RSS}}$	$\gamma_{\text{twf}}^{\text{SRO}} - \gamma_{\text{twf}}^{\text{RSS}}$
300 K	24	11	9	9.5
500 K	16	8	5	-16

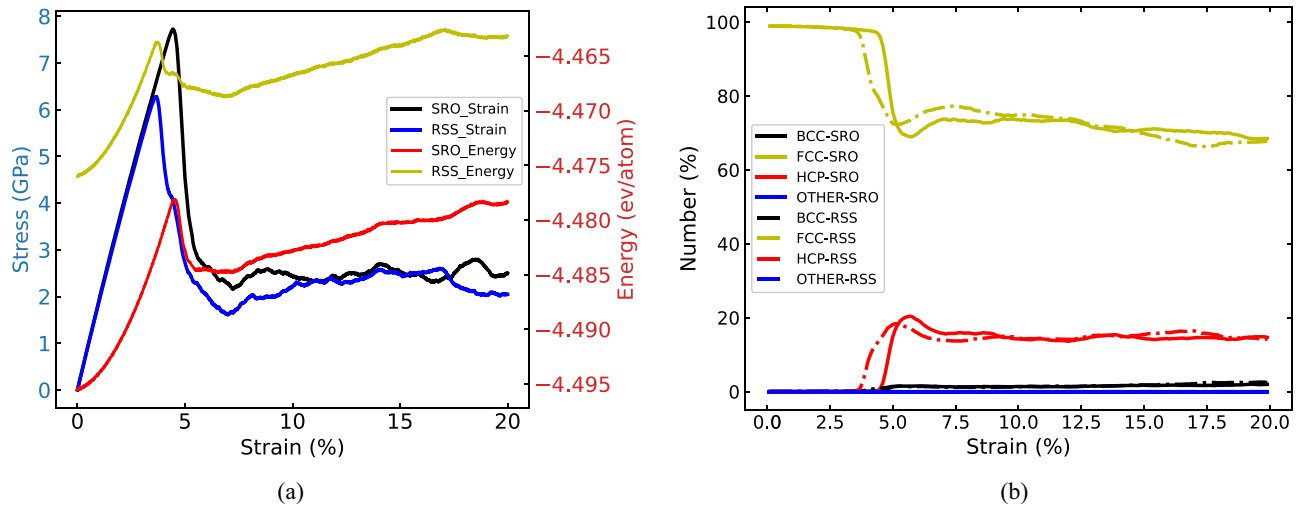


FIG. 7. Shown are the energy and stress vs strain (a) and the fraction of different types of atoms in the process of strain (b) for SRO and RSS  $\text{Co}_{30}\text{Fe}_{16.66}\text{Ni}_{36.67}\text{Ti}_{16.67}$  HEA.

Recalling the definition of  $\gamma_{\text{insf}}$  in the Ising model, the SFE is connect to the energy difference between FCC, HCP, and double HCP (DHCP) structures [71]. The decrease of SFE could suggest that the HCP structure is more energetically close to FCC phase. The concentration HCP phase changes in the slip process of incomplete dislocations. Both temperature and SRO influence the distribution of INN Co-Co and Co-Fe atomic pairs, which may stabilize the HCP phase. Additionally, with increasing temperature, the lattice distortion enhances the anti-slip ability of Shockley particles and makes shearing more difficult. Ultimately the severe local lattice distortion could lead to the elevation of GSFE.

#### D. Effect of SRO on mechanical performance

##### 1. Tensile properties of single crystalline Co-Fe-Ni-Ti

From the energy change presented in Fig. 7(a), we observe that the average energy per atom of SRO configuration for  $\text{Co}_{30}\text{Fe}_{16.66}\text{Ni}_{36.67}\text{Ti}_{16.67}$  remains more negative than the RSS structure throughout the entire tensile deformation process. It means that the SRO configuration is more stable than RSS in the process of tensile deformation. The mechanical response during tensile deformation could be characterized by three typical stages composed of the elastic zone, the yield zone, and the plastic zone. In the stage of elastic strain, the stress increases linearly. The atomic spacing of the system scales proportionally, while the lattice arrangement remains unchanged. Then, the stress experiences a sharp decline at a strain of approximately 4.43% for SRO and 3.64% for RSS [see Fig. 7(a)]. This decline suggests that SRO enhances both the strength and ductility of Co-Fe-Ni-Ti HEA. The sudden drop of stress results from the sliding of atoms within HEA, leading to the generation of a large number of HCP-type atoms and subsequently the formation of BCC-type atoms, creating the stacking faults on specific planes. This process effectively releases the internal stress within HEA [72].

The tensile deformation results in different local atomic structures, such as HCP and BCC types, which can significantly influence the material's mechanical properties.

Figure 7(b) shows the evolution of atomic structure fractions for the  $\text{Co}_{30}\text{Fe}_{16.66}\text{Ni}_{36.67}\text{Ti}_{16.67}$  HEA during tensile testing. At the strain of 4.43% (3.62% for RSS), the HCP phase begins to emerge and rapidly increases. When the strain reaches 5.5% (4.8% for RSS), the number of HCP-type atoms reaches its peak and subsequently decreases. Finally, the proportion of HCP-type atoms forms the constant curve as a function of strain. The BCC phase begins to appear at the strain of 4.43% (3.62% for RSS), but the number of BCC-phase atoms does not increase significantly and remains in the earlier stable states. The BCC phase emerges at the interface of HCP and FCC phases and shows the relatively disordered distribution. The number of HCP-type atoms increases significantly before the strain reaches the yield point for both RSS and SRO configurations. The SRO structure shows a larger number of HCP-type atoms than the RSS configuration. SRO further influences the evolution of the phase structure, leading to the transition from FCC to BCC and HCP phases.

In the initial stages of tensile deformation [see Fig. 7(a)], the energy increases with the strain. However, prior to reaching the yield point, the system has a rapid decrease in energy, as the HCP phase emerges. This observation suggests that HCP-type atoms store more energy, leading to the sudden drop of stress. In the case of the present alloy, the HCP phase serves as the energy reservoir. The similar phenomenon was observed in the FCC  $\text{CoCuFeNiPd}$  HEA [36]. Upon entering the plastic deformation stage, the proportion of crystal-type atoms experiences minor fluctuations. From Figs. 7(a) and 7(b), we could see that SRO significantly delays the emergence of HCP and BCC phases, leading to a rapid increase of the number of HCP-type atoms, compared to RSS. Furthermore, SRO enhances the ability of HEAs to store more energy throughout the deformation process. We note that the severe lattice distortion in  $\text{AlCoCuFeNi}$  HEAs promotes the phase transformation [73]. Considering that the similar lattice distortion between SRO and RSS configurations (see Table II), we may speculate that SRO plays a key role for the hysteresis of FCC-HCP transition and the adding of HCP-type atoms. Due to the faster increase rate for HCP phase and the appearance

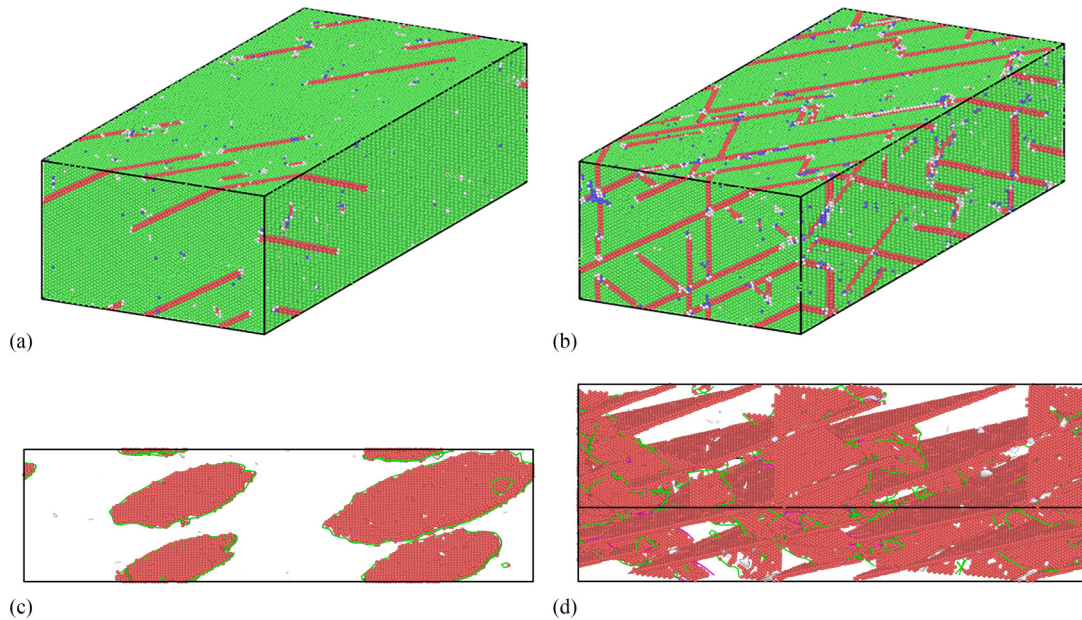


FIG. 8. Shown are the SRO and RSS configurations at 5.0% and 5.3% strain [(a) and (b)] and the stacking faults at 5.0% and 5.3% strain [(c) and (d)]. Green represent the FCC-type atoms, blue for the BCC-type atoms, and red for the HCP-type atoms.

of more HCP-type atoms in SRO configuration, SRO could store more energy before the strain yield point, delay the yield strain and enhance the yield stress. Fang *et al.* also reported that HCP phase could enhance the strength of CoCrFeMnNi HEA [74].

The changes of atomic arrangement are synergistic at the stage of elastic strain. Whereas the tensile deformation enters into the yield stage, the stacking faults appear. Along the specific plane, the large number of stacking faults quickly generate as the strain increases, as shown in Figs. 8(a) and 8(b). At this stage, the stacking faults begin to nucleate from the inside and gradually spread on the surface. As the strain gradually increases, the stacking faults appear along another direction, further these stacking faults along two directions grow and intersect with the tensile deformation. We show the numerical movies on the changes of different atoms during the tensile process (see Ref. [47]). The main types of dislocations are  $1/6\langle 112 \rangle$  Shockley incomplete dislocations. The evolution process of dislocation versus strain is shown in Fig. S4 [47]. For the FCC alloys with low SFE, the  $1/6\langle 112 \rangle$  Shockley dislocations, as the main types of dislocations, have been shown in CoCrNi HEA [41,75,76]. From Figs. 8(c) and 8(d), we could find that the occurrence of dislocations is related to the stacking faults. The increasing tensile deformation between 5.0% and 5.3% strains could induce the large change from the low density and isolated stacking faults to high density stacking faults.

In Fig. 9, it is observed that intrinsic stacking faults (ISF) experience a pronounced increase at the yield point, followed by a notable reduction in ISF-type atoms as the strain advances into the plastic deformation stage. Importantly, the twinning nucleation takes place subsequent to the emergence of ISF. The rate of twinning increase is marginally slower. The SRO configuration has more twin faults than the RSS configuration (see Fig. S5 in Ref. [47]). The lattice distortion plays a key role in facilitating twinning formation after yielding, as

well as throughout the entire strain period, by reducing the nucleation strain of Shockley partials (SPS) while increasing their resistance to propagation. Jian *et al.* reported that both LD and SRO result in the reduce of SPS movement speed, lower SPS density, and increase twinning [41]. In our alloy, there is no significant difference in LD between SRO and RSS configurations. Nevertheless, the SRO structure exhibits significantly more ISFs and twins than the RSS configuration (see Fig. 9). The SRO-induced SPS changes primarily stem from the local atomic arrangement. Twins are formed by the movement of adjacent atomic planes based on the ISF. The strain at which twins appear in the SRO and RSS configurations is identical. It could indicate that SRO does not exhibit a hysteresis effect on twinning.

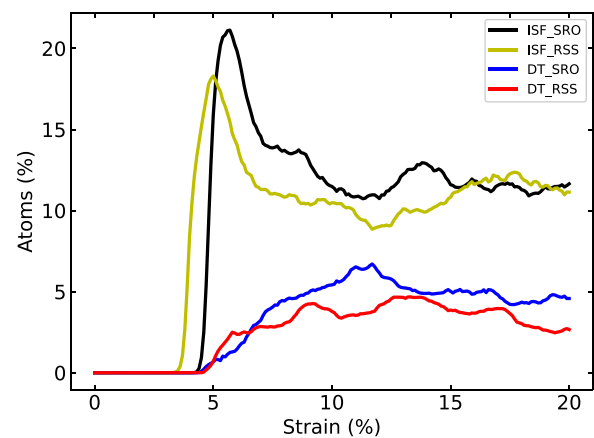


FIG. 9. Shown are the fractions of the number of atoms on the intrinsic stacking faults (ISF) and deformation twin faults (DT) for the RSS and SRO Co-Fe-Ni-Ti HEAs in the process of tensile deformation.

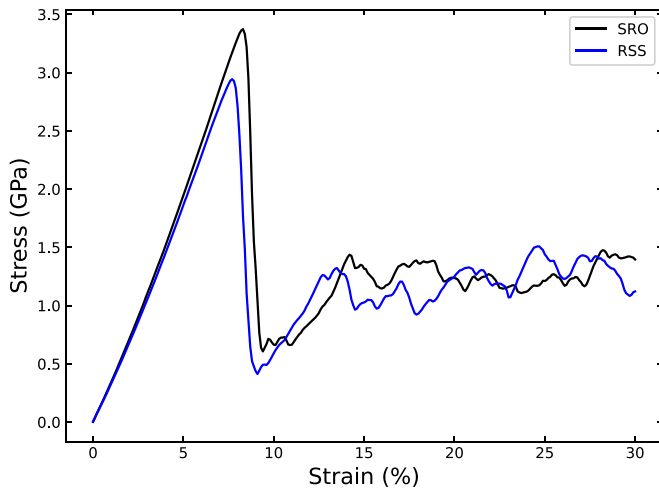


FIG. 10. The shear stress vs strain for RSS and SRO Co-Fe-Ni-Ti HEA.

Figure 9 demonstrates that the increase of ISF becomes constrained as the deformation reaches a certain strain. The deformation twins (DT) emerge at this critical strain, corresponding to the peak number of ISF. When ISF propagate, the development of DT serves to impede deformation ( $\gamma_{\text{isf}} < \gamma_{\text{twf}}$  showing in Fig. 6) and contributes to the continuous enhancement of plasticity. There are two key mechanisms on DT. First, DT regulate the crystal orientation, activate the slip, and stimulate the interplay between slip and twinning. Second, DT reduce the average free path of dislocations, leading to increased strain hardening and improved plasticity, a phenomenon known as the twinning-induced plasticity (TWIP) effect. In the SRO structure, the length of dislocation line shortens due to the challenges in unfolding stacking faults and the interaction between upper faults in different directions. Consequently, the higher dislocation density is observed, requiring greater resistance for the material to undergo plastic deformation. The dislocation density in the SRO model significantly exceeds that of the RSS configuration, resulting in more dislocation loops and nodes, which could further hinder the subsequent deformation and enhance the material's strength.

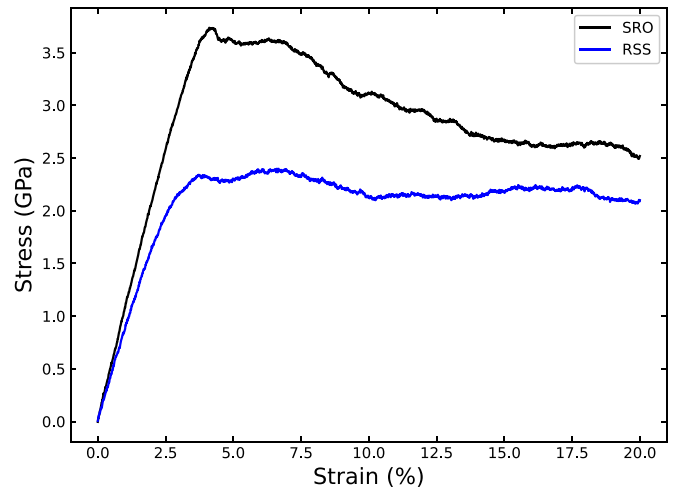


FIG. 12. The tensile strength vs strain of polycrystalline  $\text{Co}_{30}\text{Fe}_{16.66}\text{Ni}_{36.67}\text{Ti}_{16.67}$  HEA.

## 2. Shear properties of single crystalline Co-Fe-Ni-Ti

We adopted the shear configuration with the crystallographic axes  $\langle 112 \rangle$ ,  $\langle \bar{1}\bar{1}1 \rangle$ , and  $\langle 1\bar{1}0 \rangle$ . The SRO configurations with the 72 0000 atoms were predicted by using the MC/MD simulation. Subsequently, the shear deformation is expanded along the  $X$ ,  $Y$ , and  $Z$  axes by a factor of  $3 \times 3 \times 3$ , resulting in a total of 1 944 000 atoms. Figure 10 shows the shear stress-strain curves of RSS and SRO configurations for Co-Fe-Ni-Ti HEA. The shear strength reaches 2.94 GPa at a strain of 7% for RSS and 3.375 GPa at a strain of 8% for the SRO configuration. The shear modulus is 32.73 GPa for RSS and 34.47 GPa for SRO. Both the shear strength and shear modulus are enhanced, while the shear strain is delayed by SRO, thereby SRO could improve the shear performance. In RSS, the stacking faults emerge along specific planes and gradually propagate across the entire plane, as the shear stress reaches a certain threshold. This behavior is depicted in Figs. 11(a) and 11(b). The SRO exhibits the similar extension of stacking faults, but the increased SFE in SRO configuration contributes to enhanced shear strength. The analysis of atomic stress at 30% shear strain indicates that RSS contains more shear bands compared to SRO configuration. However, the average atomic shear stress in RSS configuration is smaller than that in

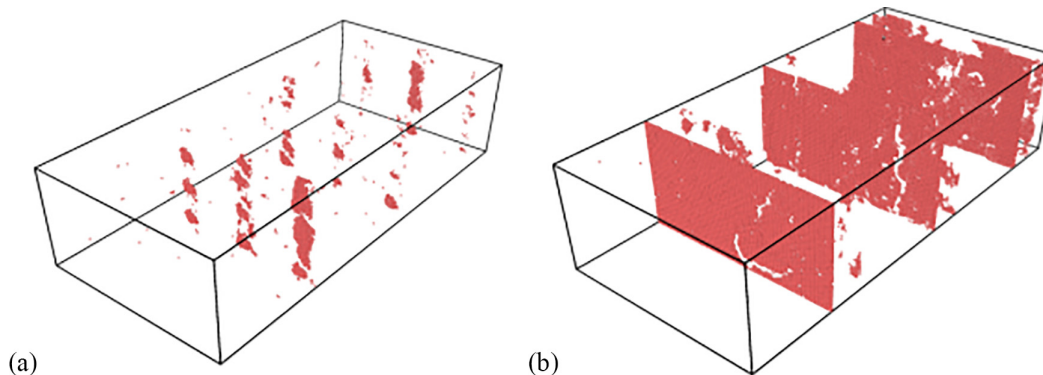


FIG. 11. The early stage of SF at the shear deformation of 8.3% for RSS (a) and the complete extension process of SF at the shear strain of 8.9% for RSS (b). The red atomic layers stand for the stacking faults.

TABLE V. Statistics of the number of metallic elements at the grain boundaries for polycrystalline  $\text{Co}_{30}\text{Fe}_{16.66}\text{Ni}_{36.67}\text{Ti}_{16.67}$  HEA.

Model	Co	Fe	Ni	Ti
SRO	0.186	0.288	0.291	0.235
RSS	0.295	0.163	0.370	0.172

SRO configuration. This difference arises from the RSS configuration consisting of 44 atomic layers with multiple shear bands collectively accommodating shear deformation, while the SRO configuration comprises only 30 atomic layers (see Fig. S6 in Ref. [47]).

### 3. Tensile properties of polycrystalline Co-Fe-Ni-Ti

The polycrystalline configuration of  $\text{Co}_{30}\text{Fe}_{16.66}\text{Ni}_{36.67}\text{Ti}_{16.67}$  with random orientations of eight grains was established by ATOMSK (see Fig. S7 in Ref. [47]). We show some polycrystalline structures with RSS and SRO predicted via the simulated annealing, respectively [see Figs. S7(b) and S7(c)]. The SRO parameters of polycrystalline and single crystalline are consistent with each other (see Figs. 1 and S8). It indicates that for RSS the polycrystalline treatment has no an important affect on the localized distribution of atoms.

The stress-strain curve of polycrystalline Co-Fe-Ni-Ti is shown in Fig. 12. With the continuous loading of strain, the stress of RSS reaches the highest point of 2.365 GPa at the tensile strain of 3.83%, while the stress of SRO reaches a maximum about 3.718 GPa at the strain of 4.25%. Obviously SRO enhances the strength and ductility of polycrystalline configuration. The deformation of each grain in polycrystalline configuration is synergistic but inconsistent, due to the different size of grains. Therefore the critical plastic strain of each grain is different. It could lead to the stress-strain curve without significant stress drop point for polycrystalline Co-Fe-Ni-Ti HEA.

The tensile elastic modulus (Young's modulus) was obtained by calculating the stress-strain curve at the linear stage. The Young's modulus of 105 GPa for SRO is larger of

25% than the value of 85 GPa for the RSS configuration. It could suggest that the improvement of mechanical properties by SRO is also applicable to the polycrystalline configurations. We note that SRO obviously improves the mechanical properties of polycrystalline  $\text{Al}_{0.3}\text{CoCrFeNi}$  HEA [77]. The present polycrystalline  $\text{Co}_{30}\text{Fe}_{16.66}\text{Ni}_{36.67}\text{Ti}_{16.67}$  HEA satisfies the anti-Hall Patch relationship [78,79] between the strength and grain size. Our simulated tensile strength of polycrystalline system is much smaller than that of the single crystalline configuration.

In the process of MC exchange for polycrystalline configurations, the rearrangement of atoms along grain boundaries could result in segregation, further could reduce the grain boundary energy. Table V lists that the atomic distribution on the grain boundary for RSS configuration, which is close to the overall element proportion of HEA. The metallic elements on the grain boundary are also randomly distributed during the tensile deformation. For SRO, the proportion of atoms at the grain boundary is very different from that of RSS. The proportion of Co atoms at the grain boundary decreases by 11%, and the Ni atoms decrease by 8%, while the proportion of Fe atoms at the grain boundary increases by 12.5%, and the Ti atoms increase by 6.3%. The SRO induced precipitation of elements at grain boundaries could further enhance the strength from 2.365 to 3.718 GPa for  $\text{Co}_{30}\text{Fe}_{16.66}\text{Ni}_{36.67}\text{Ti}_{16.67}$ . It has been reported that the precipitates obtained through hot working could increase the strength of  $\text{Al}_{0.3}\text{CoCrFeNi}$  HEA [80,81].

The CNA results shown in Fig. 13 suggest that the BCC phase in polycrystalline configurations mainly grow around grain boundaries due to the rearrangement of metallic elements, while the growth of BCC phase in single crystalline is irregular. The growth trend of HCP phase in HEAs is the similar to that of single crystalline. The SRO makes the emergence of HCP phase hysteretic, but the HCP phase in SRO configuration could appear and grow rapidly when the strain load reaches 3.8% (2.37% for RSS) shown in Fig. 14. The number of HCP-type atoms in SRO configuration exceeds that of RSS when the tensile strain is up to 5%. The energy buffer effect of HCP phase is also applicable in polycrystalline Co-Fe-Ni-Ti configurations. The HCP-phase induced more stacking faults

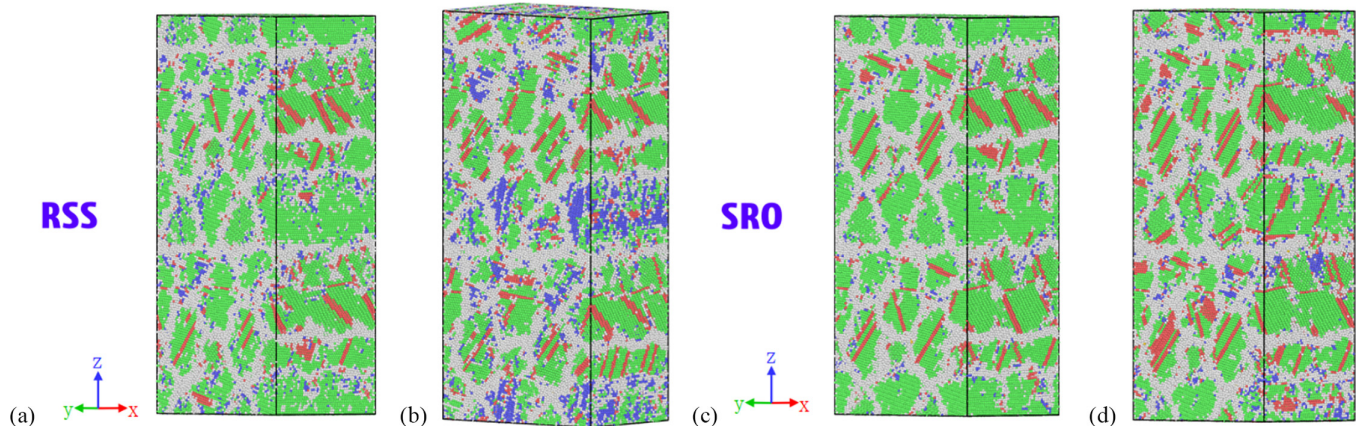


FIG. 13. Crystal structure changes at the tensile strain of 7.2% and 10.2% for the RSS model [(a) and (b)] and the SRO model [(c) and (d)]. The green represent the FCC-type atoms, blue for BCC-type atoms, red for HCP-type atoms, white for other type atoms.

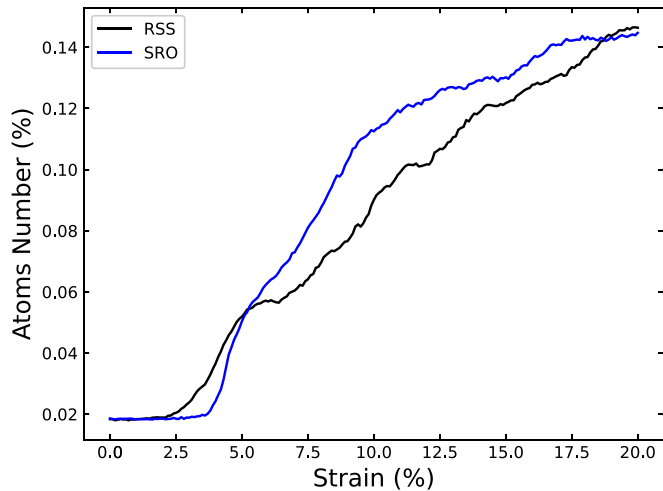


FIG. 14. The number of HCP-type atoms as a function of tensile strain for polycrystalline  $\text{Co}_{30}\text{Fe}_{16.66}\text{Ni}_{36.67}\text{Ti}_{16.67}$  HEA.

in SRO configuration further enhance the ductility, compared to those of RSS.

From Fig. 13, we could see the parallel SFs within the grains, which are different from the intersecting SFs in single crystalline. The more SFs in SRO are further confirmed, compared to those in RSS. When the strain is loaded to 10.2%, the grain boundaries of the polycrystalline configuration prevent the growth and expansion of stacking faults. The ISFs in SRO configuration grow inside the grains and gradually gather together to form the plate-like HCP phase. Compared with the subsequent plane slip and dislocation movement, this lath HCP has a greater blocking effect than twins, which further improves the strength of material. It could also mean that the deformation mechanism changes from TWIP to the transformation induced plasticity (TRIP) [77].

#### IV. CONCLUSION

Using the combination of classical molecular dynamics and Monte Carlo simulations, we have studied the short-range order (SRO) and investigated its effects on the lattice distortion, general stacking fault energy, and tensile and shear

strength for the single crystalline and polycrystalline FCC  $\text{Co}_{30}\text{Fe}_{16.66}\text{Ni}_{36.67}\text{Ti}_{16.67}$  HEA at finite temperature.

The obvious SRO of Ti-Fe and Ti-Co atomic pairs at even high annealing temperature occur in Co-Fe-Ni-Ti alloys. The nonlinear increase of lattice distortion as a function of temperature is obtained by subtracting the thermal vibration induced atomic displacement based on the Debye model. Whereas the atomic displacement away from ideal lattice site, the difference of atomic pairs, and the Voronoi tessellation parameters indicate that the local lattice distortion near metallic elements is extremely complicated. As the temperature rises, the general stacking fault energy increases. The SRO could enhance substantially the unstable stacking fault energy, while increases slightly the intrinsic stacking fault energy, but tunes the small decrease of the twin stacking energy at high temperature.

SRO could improve the mechanical behavior of single crystalline and polycrystalline Co-Fe-Ni-Ti HEA. The SRO increases the degree of deformation twinning and the number of dislocations in the single crystalline configuration, makes the number of HCP-type atoms increase, and delays the appearance of the HCP phase. As the energy buffer, the HCP phase could improve the storage capacity of dislocations and tunes the tensile and shear strength and plasticity of FCC Co-Fe-Ni-Ti HEA. In the polycrystalline configuration, SRO could promote the precipitation of BCC phases at the grain boundaries, while increase the number of HCP phases in the grains and activate the deformation of slip planes within the grains.

#### ACKNOWLEDGMENTS

This work was supported by the National Natural Science Foundation of China (Grants No. 52371174, No. 51771015, No. U1804123, and No. 51401014) and the Science Challenge Project (Grant No. TZ2018002). SHQ acknowledges the Natural Science Foundation of Henan (Grant No. 232300420126). We would like to thank D.-Y. Lin at the software center of CAEP for the molecular dynamics stimulating discussion.

The authors declare no competing interests.

- [1] J.-W. Yeh, S.-K. Chen, S.-J. Lin, J.-Y. Gan, T.-S. Chin, T.-T. Shun, C.-H. Tsau, and S.-Y. Chang, Nanostructured high-entropy alloys with multiple principal elements: Novel alloy design concepts and outcomes, *Adv. Eng. Mater.* **6**, 299 (2004).
- [2] B. Cantor, I. Chang, P. Knight, and A. Vincent, Microstructural development in equiatomic multicomponent alloys, *Mater. Sci. Eng., A* **375-377**, 213 (2004).
- [3] Y. Zhang, T. Zuo, Z. Tang, M. Gao, K. Dahmen, P. Liaw, and Z. Lu, Microstructures and properties of high-entropy alloys, *Prog. Mater. Sci.* **61**, 1 (2014).
- [4] M. C. Gao, J.-W. Yeh, P. K. Liaw, Y. Zhang *et al.*, *High-Entropy Alloys* (Cham, Springer International Publishing, 2016).
- [5] B. S. Murty, J.-W. Yeh, S. Ranganathan, and P. Bhattacharjee, *High-Entropy Alloys* (Elsevier, 2019).
- [6] F. X. Zhang, S. Zhao, K. Jin, H. Xue, G. Velisa, H. Bei, R. Huang, J. Y. P. Ko, D. C. Pagan, J. C. Neuefeind, W. J. Weber, and Y. Zhang, Local structure and short-range order in a NiCoCr solid solution alloy, *Phys. Rev. Lett.* **118**, 205501 (2017).
- [7] M. Fedorov, J. S. Wróbel, A. Fernández-Caballero, K. J. Kurzydłowski, and D. Nguyen-Manh, Phase stability and magnetic properties in fcc Fe-Cr-Mn-Ni alloys from first-principles modeling, *Phys. Rev. B* **101**, 174416 (2020).
- [8] R. Zhang, S. Zhao, J. Ding, Y. Chong, T. Jia, and C. Ophus, Short-range order and its impact on the CrCoNi medium-entropy alloy, *Nature (London)* **581**, 283 (2020).

- [9] F. G. Coury, C. Miller, R. Field, and M. Kaufman, On the origin of diffuse intensities in fcc electron diffraction patterns, *Nature (London)* **622**, 742 (2023).
- [10] B. Yin, S. Yoshida, N. Tsuji, and W. A. Curtin, Yield strength and misfit volumes of NiCoCr and implications for short-range-order, *Nat. Commun.* **11**, 2507 (2020).
- [11] Q. Ding, Y. Zhang, X. Chen, X. Fu, D. Chen, S. Chen, L. Gu, F. Wei, H. Bei, Y. Gao, M. Wen, J. Li, Z. Zhang, T. Zhu, R. O. Ritchie, and Q. Yu, Tuning element distribution, structure and properties by composition in high-entropy alloys, *Nature (London)* **574**, 223 (2019).
- [12] X. Sun, S. Lu, R. Xie, X. An, W. Li, T. Zhang, C. Liang, X. Ding, Y. Wang, H. Zhang, and L. Vitos, Can experiment determine the stacking fault energy of metastable alloys? *Mater. Des.* **199**, 109396 (2021).
- [13] M. Shih, J. Miao, M. Mills, and M. Ghazisaeidi, Stacking fault energy in concentrated alloys, *Nat. Commun.* **12**, 3590 (2021).
- [14] S. Huang, W. Li, S. Lu, F. Tian, J. Shen, E. Holmström, and L. Vitos, Temperature dependent stacking fault energy of FeCr-CoNiMn high entropy alloy, *Scr. Mater.* **108**, 44 (2015).
- [15] L. Zhu and Z. Wu, Effects of short range ordering on the generalized stacking fault energy and deformation mechanisms in FCC multiprincipal element alloys, *Acta Mater.* **259**, 119230 (2023).
- [16] H. Song, F. Tian, Q.-M. Hu, L. Vitos, Y. Wang, J. Shen, and N. Chen, Local lattice distortion in high-entropy alloys, *Phys. Rev. Mater.* **1**, 023404 (2017).
- [17] Q. He and Y. Yang, On lattice distortion in high entropy alloys, *Frontiers in Materials* **5**, 42 (2018).
- [18] O. L. Robert and J. N. Gwilym, Lattice distortions in high-entropy alloys, *J. Mater. Res.* **33**, 2954 (2018).
- [19] W. Liu, X.-G. Lu, and Q.-M. Hu, Comprehensive understanding of local lattice distortion in dilute and equiatomic FCC alloys, *Mater. Chem. Phys.* **293**, 126928 (2023).
- [20] J. Ding, Q. Yu, M. Asta, and R. O. Ritchie, Tunable stacking fault energies by tailoring local chemical order in CrCoNi medium-entropy alloys, *Proc. Natl. Acad. Sci.* **115**, 8919 (2018).
- [21] M. Radhakrishnan, M. McKinstry, V. Chaudhary, M. S. Nartu, K. V. Krishna, R. V. Ramanujan, R. Banerjee, and N. B. Dahotre, Effect of chromium variation on evolution of magnetic properties in laser direct energy additively processed CoCrFeNi alloys, *Scr. Mater.* **226**, 115269 (2023).
- [22] T. A. Elmslie, J. Startt, S. Soto-Medina, Y. Yang, K. Feng, R. E. Baumbach, E. Zappala, G. D. Morris, B. A. Frandsen, M. W. Meisel, M. V. Manuel, R. Dingreville, and J. J. Hamlin, Magnetic properties of equiatomic CrMnFeCoNi, *Phys. Rev. B* **106**, 014418 (2022).
- [23] X. Zhou, H. Wadley, R. Johnson, D. Larson, N. Taba, A. Cerezo, A. Petford-Long, G. Smith, P. Clifton, R. Martens, and T. Kelly, Atomic scale structure of sputtered metal multilayers, *Acta Mater.* **49**, 4005 (2001).
- [24] S. I. Rao, C. Woodward, T. A. Parthasarathy, and O. Senkov, Atomistic simulations of dislocation behavior in a model FCC multicomponent concentrated solid solution alloy, *Acta Mater.* **134**, 188 (2017).
- [25] E. Antillon, C. Woodward, S. Rao, and B. Akdim, Chemical short range order strengthening in BCC complex concentrated alloys, *Acta Mater.* **215**, 117012 (2021).
- [26] Y. Niu, D. Zhao, B. Zhu, S. Wang, Z. Wang, and H. Zhao, Investigations on the role of chemical short-range order in the tensile deformation of FCC  $\text{Co}_{30}\text{Fe}_{16.67}\text{Ni}_{36.67}\text{Ti}_{16.67}$  high-entropy alloys via Monte Carlo and molecular dynamics hybrid simulations, *Comput. Mater. Sci.* **215**, 111787 (2022).
- [27] J. Ren, W. Li, Q. Wang, R. Yang, Q. Gao, J. Li, H. Xue, X. Lu, and F. Tang, Atomistic simulation of tribology behaviors of Ti-based FeCoNiTi high entropy alloy coating during nano-scratching, *Vacuum* **213**, 112124 (2023).
- [28] E. Antillon, C. Woodward, S. Rao, B. Akdim, and T. Parthasarathy, Chemical short range order strengthening in a model FCC high entropy alloy, *Acta Mater.* **190**, 29 (2020).
- [29] M. S. Lucas, G. B. Wilks, L. Mauger, J. A. Muñoz, O. N. Senkov, E. Michel, J. Horwath, S. L. Semiatin, M. B. Stone, D. L. Abernathy, and E. Karapetrova, Absence of long-range chemical ordering in equimolar FeCoCrNi, *Appl. Phys. Lett.* **100**, 251907 (2012).
- [30] F. Tian, H. Zhao, Y. Wang, and N. Chen, Investigating effect of ordering on magnetic-elastic property of FeNiCoCr medium-entropy alloy, *Scr. Mater.* **166**, 164 (2019).
- [31] Y. Zhang, G. M. Stocks, K. Jin, C. Lu, H. Bei, B. C. Sales, L. Wang, L. K. Béland, R. E. Stoller, G. D. Samolyuk, M. Caro, A. Caro, and W. J. Weber, Influence of chemical disorder on energy dissipation and defect evolution in concentrated solid solution alloys, *Nat. Commun.* **6**, 8736 (2015).
- [32] S. Wang, S. Chen, Y. Jia, Z. Hu, H. Huang, Z. Yang, A. Dong, G. Zhu, D. Wang, D. Shu, F. Tian, Y. Dai, and B. Sun, FCC-L12 ordering transformation in equimolar FeCoNiV multi-principal element alloy, *Mater. Des.* **168**, 107648 (2019).
- [33] S. S. Sohn, A. Kwiatkowski da Silva, Y. Ikeda, F. Körmann, W. Lu, W. S. Choi, B. Gault, D. Ponge, J. Neugebauer, and D. Raabe, Ultrastrong medium-entropy single-phase alloys designed via severe lattice distortion, *Adv. Mater.* **31**, 1807142 (2019).
- [34] X. Chen, Q. Wang, Z. Cheng, M. Zhu, H. Zhou, P. Jiang, L. Zhou, Q. Xue, F. Yuan, J. Zhu, X. Wu, and E. Ma, Direct observation of chemical short-range order in a medium-entropy alloy, *Nature (London)* **592**, 712 (2021).
- [35] Q.-J. Li, H. Sheng, and E. Ma, Strengthening in multi-principal element alloys with local-chemical-order roughened dislocation pathways, *Nat. Commun.* **10**, 3563 (2019).
- [36] S. Chen, Z. H. Aitken, S. Pattamatta, Z. Wu, Z. G. Yu, D. J. Srolovitz, P. K. Liaw, and Y.-W. Zhang, Simultaneously enhancing the ultimate strength and ductility of high-entropy alloys via short-range ordering, *Nat. Commun.* **12**, 4953 (2021).
- [37] C. D. Woodgate and J. B. Staunton, Short-range order and compositional phase stability in refractory high-entropy alloys via first-principles theory and atomistic modeling: NbMoTa, NbMoTaW, and VNbMoTaW, *Phys. Rev. Mater.* **7**, 013801 (2023).
- [38] S. Yin, J. Ding, M. Asta, and R. O. Ritchie, *Ab initio* modeling of the energy landscape for screw dislocations in body-centered cubic high-entropy alloys, *npj Comput. Mater.* **6**, 110 (2020).
- [39] B. Zhang, J. Ding, and E. Ma, Chemical short-range order in body-centered-cubic TiZrHfNb high-entropy alloys, *Appl. Phys. Lett.* **119**, 201908 (2021).
- [40] T. Shi, Z. Su, J. Li, C. Liu, J. Yang, X. He, D. Yun, Q. Peng, and C. Lu, Distinct point defect behaviours in body-centered cubic medium-entropy alloy NbZrTi induced by severe lattice distortion, *Acta Mater.* **229**, 117806 (2022).

- [41] W.-R. Jian, Z. Xie, S. Xu, Y. Su, X. Yao, and I. J. Beyerlein, Effects of lattice distortion and chemical short-range order on the mechanisms of deformation in medium entropy alloy CoCrNi, *Acta Mater.* **199**, 352 (2020).
- [42] P. Singh, A. V. Smirnov, and D. D. Johnson, Atomic short-range order and incipient long-range order in high-entropy alloys, *Phys. Rev. B* **91**, 224204 (2015).
- [43] P.-Y. Cao, J. Wang, P. Jiang, Y.-J. Wang, F.-P. Yuan, and X.-L. Wu, Prediction of chemical short-range order in high-/medium-entropy alloys, *J. Mater. Sci. Technol.* **169**, 115 (2024).
- [44] A. Stukowski, Visualization and analysis of atomistic simulation data with ovito—the open visualization tool, *Modell. Simul. Mater. Sci. Eng.* **18**, 015012 (2010).
- [45] P. Hirel, ATOMSK: A tool for manipulating and converting atomic data files, *Comput. Phys. Commun.* **197**, 212 (2015).
- [46] F. Tian, D.-Y. Lin, X. Gao, Y.-F. Zhao, and H.-F. Song, A structural modeling approach to solid solutions based on the similar atomic environment, *J. Chem. Phys.* **153**, 034101 (2020).
- [47] See Supplemental Material at <http://link.aps.org/supplemental/10.1103/PhysRevMaterials.8.053602> for the energy vs volume curve, potential energy vs step of MC simulation, lattice distortion at different temperatures, different-type dislocation lines, stacking faults, atomic stress diagrams, schematic diagrams of polycrystalline, and SRO parameters of polycrystalline.
- [48] N. Metropolis, A. W. Rosenbluth, M. N. Rosenbluth, A. H. Teller, and E. Teller, Equation of state calculations by fast computing machines, *J. Chem. Phys.* **21**, 1087 (1953).
- [49] K. Lonsdale, Vibration amplitudes of atoms in cubic crystals, *Acta Crystallogr.* **1**, 142 (1948).
- [50] H. H. Pham, M. E. Williams, P. Mahaffey, M. Radovic, R. Arroyave, and T. Cagin, Finite-temperature elasticity of fcc Al: Atomistic simulations and ultrasonic measurements, *Phys. Rev. B* **84**, 064101 (2011).
- [51] S. Huang, F. Tian, and L. Vitos, Elasticity of high-entropy alloys from *ab initio* theory, *J. Mater. Res.* **33**, 2938 (2018).
- [52] D. de Fontaine, The number of independent pair-correlation functions in multicomponent systems, *J. Appl. Crystallogr.* **4**, 15 (1971).
- [53] A. V. Ceguerra, R. C. Powles, M. P. Moody, and S. P. Ringer, Quantitative description of atomic architecture in solid solutions: A generalized theory for multicomponent short-range order, *Phys. Rev. B* **82**, 132201 (2010).
- [54] J. M. Cowley, X-ray measurement of order in single crystals of Cu<sub>3</sub>Au, *J. Appl. Phys.* **21**, 24 (1950).
- [55] C. Varvenne, A. Luque, W. G. Nöhring, and W. A. Curtin, Average-atom interatomic potential for random alloys, *Phys. Rev. B* **93**, 104201 (2016).
- [56] S. Kang and A. Tamm, Density functional study of atomic arrangements in CrMnFeCoNi high-entropy alloy and their impact on vacancy formation energy and segregation, *Comput. Mater. Sci.* **230**, 112456 (2023).
- [57] Y. Wu, F. Zhang, X. Yuan, H. Huang, X. Wen, Y. Wang, M. Zhang, H. Wu, X. Liu, H. Wang, S. Jiang, and Z. Lu, Short-range ordering and its effects on mechanical properties of high-entropy alloys, *J. Mater. Sci. Technol.* **62**, 214 (2021).
- [58] H. Ge and F. Tian, A review of *ab initio* calculation on lattice distortion in high-entropy alloys, *JOM* **71**, 4225 (2019).
- [59] F. Tian, L. K. Varga, N. Chen, J. Shen, and L. Vitos, Empirical design of single phase high-entropy alloys with high hardness, *Intermetallics* **58**, 1 (2015).
- [60] S. Guo, C. Ng, J. Lu, and C. T. Liu, Effect of valence electron concentration on stability of fcc or bcc phase in high entropy alloys, *J. Appl. Phys.* **109**, 103505 (2011).
- [61] Y.-Y. Tan, T. Li, Y. Chen, Z.-J. Chen, M.-Y. Su, J. Zhang, Y. Gong, T. Wu, H.-Y. Wang, and L.-H. Dai, Uncovering heterogeneity of local lattice distortion in TiZrHfNbTa refractory high entropy alloy by SR-XRD and EXAFS, *Scr. Mater.* **223**, 115079 (2023).
- [62] L. Owen, N. Jones, H. Stone, and H. Playford, Separation of static and dynamic displacements in the CrMnFeCoNi high entropy alloy, *Acta Mater.* **262**, 119164 (2024).
- [63] B. Chen, S. Li, J. Ding, X. Ding, J. Sun, and E. Ma, Correlating dislocation mobility with local lattice distortion in refractory multi-principal element alloys, *Scr. Mater.* **222**, 115048 (2023).
- [64] Y.-Y. Tan, M.-Y. Su, Z.-C. Xie, Z.-J. Chen, Y. Gong, L.-R. Zheng, Z. Shi, G. Mo, Y. Li, L.-W. Li *et al.*, Chemical composition dependent local lattice distortions and magnetism in high entropy alloys, *Intermetallics* **129**, 107050 (2021).
- [65] H. Wang, Q. He, A. Wang, and Y. Yang, Tuning Elinvar effect in severely distorted single-phase high entropy alloys, *J. Appl. Phys.* **133**, 055105 (2023).
- [66] H. Wang, Q. He, X. Gao, Y. Shang, W. Zhu, W. Zhao, Z. Chen, H. Gong, and Y. Yang, Multifunctional high entropy alloy enabled by severe lattice distortion, *Adv. Mater.* **36**, 2305453 (2023).
- [67] L. Casillas-Trujillo, B. Osinger, R. Lindblad, D. Karlsson, A. I. Abrikosov, S. Fritze, K. Von Fieandt, B. Alling, I. Hotz, U. Jansson, I. A. Abrikosov, and E. Lewin, Experimental and theoretical evidence of charge transfer in multi-component alloys-how chemical interactions reduce atomic size mismatch, *Mater. Chem. Front.* **5**, 5746 (2021).
- [68] X. Zhang, B. Grabowski, F. Körmann, A. V. Ruban, Y. Gong, R. C. Reed, T. Hickel, and J. Neugebauer, Temperature dependence of the stacking-fault Gibbs energy for Al, Cu, and Ni, *Phys. Rev. B* **98**, 224106 (2018).
- [69] S. Zhao, G. M. Stocks, and Y. Zhang, Stacking fault energies of face-centered cubic concentrated solid solution alloys, *Acta Mater.* **134**, 334 (2017).
- [70] L. Rémy, A. Pineau, and B. Thomas, Temperature dependence of stacking fault energy in close-packed metals and alloys, *Mater. Sci. Eng.* **36**, 47 (1978).
- [71] L. Vitos, *Computational Quantum Mechanics for Materials Engineers* (Springer-Verlag, 2007).
- [72] X. Liu, H. Zhao, H. Ding, D.-Y. Lin, and F. Tian, Effect of short-range order on the mechanical behaviors of tensile and shear for NiCoFeCr, *Appl. Phys. Lett.* **119**, 131904 (2021).
- [73] Y.-C. Wu and J.-L. Shao, FCC-BCC phase transformation induced simultaneous enhancement of tensile strength and ductility at high strain rate in high-entropy alloy, *Int. J. Plast.* **169**, 103730 (2023).
- [74] Q. Fang, Y. Chen, J. Li, C. Jiang, B. Liu, Y. Liu, and P. K. Liaw, Probing the phase transformation and dislocation evolution in dual-phase high-entropy alloys, *Int. J. Plast.* **114**, 161 (2019).
- [75] C. Liu, Y. Yang, and Z. Xia, Deformation mechanism in Al<sub>0.1</sub>CoCrFeNi<sub>3</sub> (111)[110] high entropy alloys—molecular dynamics simulations, *RSC Adv.* **10**, 27688 (2020).

- [76] M. Bahramyan, R. T. Mousavian, and D. Brabazon, Study of the plastic deformation mechanism of trip–twip high entropy alloys at the atomic level, *Int. J. Plast.* **127**, 102649 (2020).
- [77] Z. Sun, C. Shi, C. Liu, H. Shi, and J. Zhou, The effect of short-range order on mechanical properties of high entropy alloy  $\text{Al}_{0.3}\text{CoCrFeNi}$ , *Mater. Des.* **223**, 111214 (2022).
- [78] Y. Qi, M. Zhao, and M. Feng, Molecular simulation of microstructure evolution and plastic deformation of nanocrystalline  $\text{CoCrFeMnNi}$  high-entropy alloy under tension and compression, *J. Alloys Compd.* **851**, 156923 (2021).
- [79] A. G. Sheinerman, R. H. Castro, and M. Y. Gutkin, A model for direct and inverse Hall-Petch relation for nanocrystalline ceramics, *Mater. Lett.* **260**, 126886 (2020).
- [80] B. Gwalani, V. Soni, M. Lee, S. Mantri, Y. Ren, and R. Banerjee, Optimizing the coupled effects of Hall-Petch and precipitation strengthening in a  $\text{Al}_{0.3}\text{CoCrFeNi}$  high entropy alloy, *Mater. Des.* **121**, 254 (2017).
- [81] B. Gwalani, S. Gorsse, D. Choudhuri, Y. Zheng, R. S. Mishra, and R. Banerjee, Tensile yield strength of a single bulk  $\text{Al}_{0.3}\text{CoCrFeNi}$  high entropy alloy can be tuned from 160 MPa to 1800 MPa, *Scr. Mater.* **162**, 18 (2019).